Zitierweise: *Angew. Chem. Int. Ed.* **2025**, *64*, e202423521
doi.org/10.1002/anie.202423521

Transient Porosity *Hot Paper*

A Needle in a Haystack: Transient Porosity in a Closed Pore Square Lattice Coordination Network

Kyriaki Koupepidou, Alan C. Eaby, Debobroto Sensharma, Sousa Javan Nikkhah, Tao He, Matteo Lusi, Matthias Vandichel, Leonard J. Barbour, Soumya Mukherjee, and Michael J. Zaworotko**

Abstract: Guest transport through discrete voids (closed pores) in crystalline solids is poorly understood. Herein, we report the gas sorption properties of a nonporous coordination network, $\{[Co(bib)_2Cl_2]\cdot 2MeOH\}_n$ (**sql-bib-Co-Cl-α**), featuring square lattice (**sql**) topology and the bent linker 1,3-bis(1*H*-imidazol-1-yl)benzene (bib). The as-synthesized **sql-bib-Co-Cl-α** has 11.3 % (313 Å^3) of its unit cell volume in closed pores occupied by methanol (MeOH). Upon desolvation and air exposure, **sql-bib-Co-Cl-α** underwent a single-crystal to single-crystal (SC-SC) phase transformation to **sql-bib-Co-Cl-β′**, wherein MeOH was replaced by water. Activation (vacuum or N_2 flow) resulted in dehydration and retention of the closed pores, affording **sql-bib-Co-Cl-β** with 7.7 % (194 Å^3) guest-accessible space. **sql-bib-Co-Cl-β** was found to preferentially adsorb C_2H_2 (at 265 K) over CO_2 (at 195 K) through gate-opening mechanisms, at gate-opening pressures of 59.8 and 27.7 kPa, respectively, while other C2 gases were excluded. PXRD was used to monitor transformations between the three phases of **sql-bib-Co-Cl**, while in situ DSC, in situ SCXRD under CO_2 pressure, and computational studies provided insight into the guest transport mechanism, which we attribute to the angular, flexible nature of the bib ligand. Further, the preferential adsorption of C_2H_2 over CO_2 and other C2 gases suggests that transiently porous sorbents might have utility in separations.

Introduction

Porosity is a feature of some classes of coordination networks (CNs), enabling them to perform functions that require diffusion and adsorption on a porous surface.[1a,b, c, d] Specifically related to gases, gas separation can be efficiently performed by some classes of CNs with conventional (static) porosity,[2a,b, c] typically enabled by infinite channels with a minimum diameter of ca. 3 Å.[3a,b] In such cases, permanently porous CNs (PCNs) with appropriate pore size and chemistry can selectively adsorb one gaseous compound out of a multicomponent mixture, offering in some cases ultra-high selectivities.[4a,b] Nevertheless, the ability to accommodate gas molecules can potentially occur without the existence of permanent continuous channels, porosity through "closed pores"[5] (Figure 1) enabled by "transient porosity".[3a,6] Although this concept seems counterintuitive, guest transport in molecular nonporous solids has already been established, primarily by Barrer's group[7] and then the groups of Atwood and Barbour,[8a,b,c] among others.[9a,b] On the other hand, very few studies have demonstrated that transient porosity exists in nonporous CNs.[10a,b,c]

Guest transport without permanent pores, transient porosity, requires a degree of host flexibility to enable diffusion of guest molecules.[3a] When a flexible host CN undergoes phase transformations to modify the size or shape of existing voids and enable guest diffusion then the term "*cooperative porosity*" can be employed.[3b] In some cases, these phase transformations result in S-shaped isotherms where a minimum threshold pressure is needed to induce the needed phase transformation, often resulting in a large uptake difference over a small pressure range.[11a,b,c] S-shaped isotherms remain relatively rare but are generally advantageous compared to the type I isotherms typically displayed by microporous solids. This is because they offer working capacity enhancement.[11a,12] In this context, nonporous solids are appealing as sorbents due to their potentially sigmoidal isotherm shapes when exposed to gases.[10a] Despite this, closed pore and nonporous CNs are seldom studied for their gas sorption properties, and the dearth of information is compounded by the fact that most porous CNs can be readily designed from the ground up,[13] whereas nonporous CNs that exhibit gas adsorption properties are typically discovered serendipitously rather than made by design.

Crystal engineering offers a paradigm to design CNs with desired structural features and exert control over

---

[*] Dr. K. Koupepidou, Dr. A. C. Eaby, Dr. D. Sensharma,
Dr. S. Javan Nikkhah, Dr. T. He, Prof. M. Lusi, Prof. M. Vandichel,
Prof. S. Mukherjee, Prof. M. J. Zaworotko
Bernal Institute, Department of Chemical Sciences
University of Limerick
Limerick V94 T9PX, Ireland
E-mail: soumya.mukherjee@ul.ie
xtal@ul.ie

Prof. L. J. Barbour
Department of Chemistry and Polymer Science
Stellenbosch University
Private Bag X1, Matieland 7602, South Africa

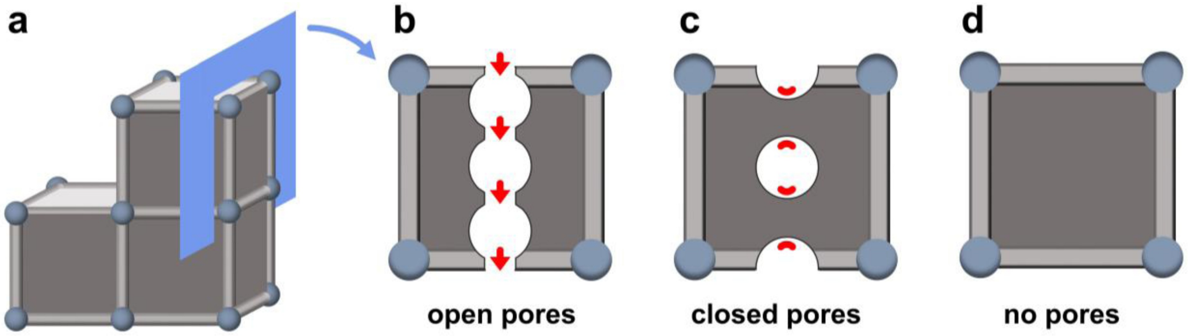

Figure 1. (a) Schematic representation of a coordination network (CN), where the blue shaded area indicates a cross-section of one unit cell. Classification of porosity in CNs based on the unit cell cross-section: (b) open pores; (c) closed pores; (d) no pores. Red arrows in (b) indicate guest transport and red lines in (c) indicate absence of a permanent guest transport pathway.

physicochemical properties.[14a,b,c] For example, node connectivity, and consequently topology, can be tuned through choice of building blocks and linker ligands.[15a,b] Recently, crystal engineering of switching CNs, i.e., CNs that undergo phase transformations from nonporous to porous phases, have become of growing interest.[16] Switching CNs are typically designed and fine-tuned through ligand[17a,b] and metal[18a,b] choice, as well as external particle properties such as particle size and crystal morphology.[19] However, the design of transiently porous CNs, i.e., CNs that undergo phase transformations from nonporous to (other) nonporous phases is in its infancy, exacerbated by the fact that most CN adsorbents are porous.

Herein, we employed the bent linker 1,3-bis(1*H*-imidazol-1-yl)benzene (bib, Scheme 1) to explore its potential to form a transiently porous CN. Although bib has been typically used to produce helical 1D chains through its *syn*-configuration,[20a,b] it has recently been studied in its *anti*-configuration in a transiently porous CN platform, **X-dmp-1-M** (M = Co, Zn, Cd), in combination with a carboxylate linker.[10b,c] In this platform, guest transport was enabled through rotation of the extended π system of the carboxylate linker, while bib acted as a secondary linker by providing subtle movement during phase transformations. A survey of bib connected to any metal using the Cambridge Structural Database (CSD, version 2024.2.0) revealed 122 hits, out of which only 5 are CNs based on bib as the only linker (CSD Refcodes IZATUA,[20a] LAYFIC,[21] WOMCAE,[22] JOMSUD[23] and JOMTAK,[23] Table S1 and Figure S1). Since its *anti*- configuration can sustain longer metal-metal distances while maintaining acute torsion angles,[24] we employed bib to produce a 2D square lattice (**sql**) network with the potential for dynamic properties, $\{[\mathrm{Co(bib)_2Cl_2}]\cdot 2\mathrm{MeOH}\}_n$ or **sql-bib-Co-Cl-α**. The unusual sorption properties of **sql-bib-Co-Cl-α** revealed transient porosity as detailed and analyzed herein.

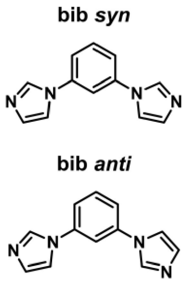

Scheme 1. *Syn*- and *anti*- configurations of the ligand 1,3-bis(1*H*-imidazol-1-yl)benzene (bib).

Results and Discussion

Synthesis and Phase Transformations

Single crystals of **sql-bib-Co-Cl-α** were obtained by layering a methanolic solution of bib onto a methanolic solution of $\mathrm{CoCl_2\cdot 6H_2O}$ and then allowing the layers to diffuse over 3 days at room temperature (Figure 2a). Single-crystal X-ray diffraction (SCXRD) revealed that **sql-bib-Co-Cl-α** had crystallized in the monoclinic space group *C*2/*c* (Table S2). The asymmetric unit is comprised of half a $\mathrm{Co^{2+}}$ cation, one $\mathrm{Cl^-}$ ligand, one bib ligand (Figure S2) and one methanol (MeOH) solvate molecule that forms a hydrogen bond with the chloro ligand (O···Cl = 3.080(2) Å). The $\mathrm{Co^{2+}}$ centers are octahedral with axial positions occupied by chloro ligands (Figure 2b). This affords 4-connected nodes that generate an **sql** network. Adjacent **sql** nets align linearly respective to the nodes (Figure 2c), but the bib linkers adopt inversed configurations following the glide plane.

The presence of solvent molecules in **sql-bib-Co-Cl-α** prompted us to investigate its response to activation. Upon heating at 333 K under vacuum and subsequent exposure to air for ca. 30 minutes, **sql-bib-Co-Cl-α** underwent a phase transformation to **sql-bib-Co-Cl-β′** coinciding with loss of MeOH (Figure 2d). SCXRD revealed that the new phase had adsorbed water from air during handling, occupying the same crystallographic locations as the MeOH solvate molecules and remaining in the same space group. The driving force behind water vapour adsorption can be attributed to hydrogen bonding between water molecules and chloro ligands (O···Cl = 3.23(1) Å) (see Supporting Information for refinement details). In addition to guest

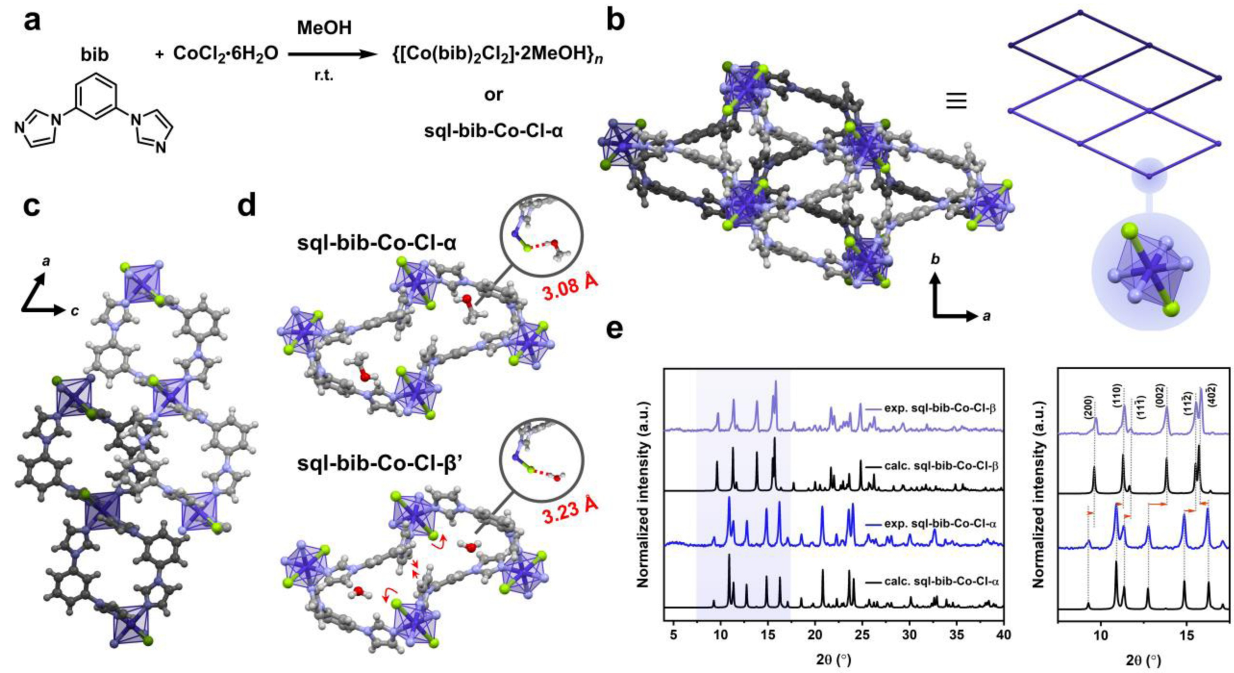

Figure 2. (a) Synthesis of {[Co(bib)$_2$Cl$_2$]·2MeOH}$_n$, **sql-bib-Co-Cl-α** (r.t. = room temperature), (b) topological analysis and crystal packing along the crystallographic *c* axis, (c) **sql** nets along the crystallographic *b* axis, (d) representation of the crystal packing and cavity chemistry in **sql-bib-Co-Cl-α** and **sql-bib-Co-Cl-β**, (e) powder X-ray diffraction and analysis of peak shifting within the range of 7.5° to 17.5° 2θ. Color codes: C, grey; H, white; N, blue; O, red; Cl, green; Co, purple. Darkened atoms in (b) and (c) represent an adjacent **sql** net.

exchange, an increase in Cl···Cl distance from 7.0201(8) Å in **sql-bib-Co-Cl-α** to 7.1182(8) Å in **sql-bib-Co-Cl-β′** moved the chloro ligands into the cavities (Figure 1d). The torsion angle between the central phenyl ring and the imidazole ring (N–N–C–C) of 22.8(7)° increased to 30.6(8)° from **α** to **β′**. The angle change caused opposite imidazole rings to move closer to each other, with the shortest C–C distance from opposite rings reducing from 3.761(3) Å to 3.459(3) Å. Even though these differences are subtle, they effectively changed the cavity limiting diameter from 2.05 Å to 1.57 Å and reduced the void space by 38.0 % (313 to 194 Å^3). Therefore, **sql-bib-Co-Cl** in effect adapts to the reduced size of the guest by an induced fit mechanism. Changes in crystal packing were also evident in the powder X-ray diffraction (PXRD) patterns of the bulk phases, with peaks shifting generally to higher 2θ angles from **α** to **β′** (Figure 2e). That the experimental PXRD patterns are consistent with the calculated patterns from the SCXRD structures demonstrated bulk phase purity. Further, **sql-bib-Co-Cl-α** could be obtained by soaking **sql-bib-Co-Cl-β′** in MeOH for 1 day, as indicated by PXRD patterns (Figure S3). Thermogravimetric analysis (TGA) showed that MeOH loss in **sql-bib-Co-Cl-α** and water loss in **sql-bib-Co-Cl-β′** were complete by 350 K, while the framework was stable up to 500 K (Figures S4 and S5).

The presence of water molecules in the voids of **sql-bib-Co-Cl-β′** motivated us to study the activation process of **sql-bib-Co-Cl-α**. A variable temperature PXRD experiment (VT PXRD) conducted under dynamic vacuum revealed that **sql-bib-Co-Cl-α** underwent transformation to **sql-bib-Co-Cl-β** (Figure 3a). The **β** form remained stable to vacuum and heat to 398 K, the temperature being above the boiling point of water (373 K). Heating above 423 K afforded a less crystalline phase following structural transformation to a phase with a similar decomposition temperature to those of the **α** and **β** phases (Figures S6 and S7). After heating to 473 K and cooling to room temperature, a color change from pink to blue was observed (Figure S8), suggesting concomitant change in the coordination sphere from octahedral to tetrahedral. Similar thermochromic behavior upon change in coordination number has been observed for other coordination compounds containing Co^{2+} centers,[25a,b] as also seen for the precursor CoCl$_2$, which is pink in its hydrated (octahedral) form but blue in its anhydrous (tetrahedral) form.[26a,b] The VT PXRD results on **sql-bib-Co-Cl-α** up to 398 K indicated a guest free phase with the same crystal packing as **sql-bib-Co-Cl-β′** (Figure 2a). Indeed, SCXRD data collected on a single crystal of **sql-bib-Co-Cl-α** heated to 333 K under nitrogen (N$_2$) flow for 30 minutes afforded guest free **sql-bib-Co-Cl-β**. This process was accompanied by a color change from pink to pale purple, along with loss of crystal transparency seen along the (100) crystal face (Figure 3b). A differential scanning calorimetry (DSC) experiment conducted under N$_2$ flow was consistent with the SCXRD experiment, revealing an endothermic peak starting at ca. 333 K, corresponding to the phase transition from **α** to **β** (Figure S9). Subsequent cycles did not exhibit any peaks, indicating that **sql-bib-Co-Cl-β** remained stable once formed. Fourier transform infrared spectroscopy (FTIR) conducted on **sql-bib-Co-Cl-α** supported MeOH

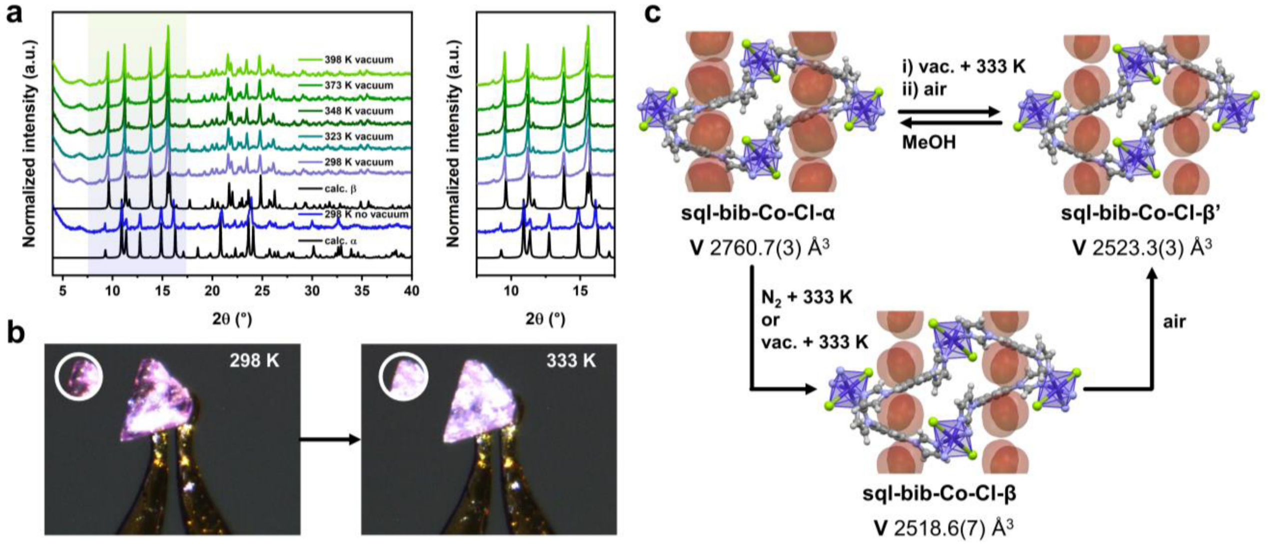

Figure 3. (a) VT PXRD patterns of **sql-bib-Co-Cl-α** under vacuum, (b) color change of a single crystal of **sql-bib-Co-Cl-α** along (100) upon activation at 333 K for 30 minutes, (c) phase conversion diagram of **sql-bib-Co-Cl**.

intermolecular hydrogen bonds, showing a broad peak at 3285 cm^{-1} (Figure S10). After heating at 333 K for 10 minutes, the MeOH peak had diminished, while a broad peak appeared at 3438 cm^{-1}, indicating the presence of water molecules. Based on these findings, a phase interconversion landscape can be constructed (Figure 3c) which summarizes the procedures used to obtain the three nonporous phases of **sql-bib-Co-Cl**: **α**, **β′** and **β**. Scanning electron microscopy (SEM) revealed that upon heating at 333 K for 12 hours, some of the larger crystals split into smaller ones, with d_{min} of 100 and 50 μm, before and after activation, respectively (Figure S11). This is expected since the stress associated with extreme phase transformations in flexible CNs is known to result in reduction of average crystallite size.[27]

The response of **sql-bib-Co-Cl** to water vapor was investigated further through a dynamic vapor sorption (DVS) experiment. A moderately hydrophilic type I isotherm[28] was observed at 300 K up to 60 % relative humidity (RH) with uptake of 5.5 wt %, corresponding to one water molecule per formula unit (Figure S12). Given that the molecular volume of H_2O ($V_g = 19$ Å^3) is much smaller than MeOH ($V_g = 37$ Å^3),[29] the linear isotherm profile can be attributed to diffusion into **sql-bib-Co-Cl-β** (Figure S13). The water uptake at low RH is also supported by the crystallographic observation of lattice water in **sql-bib-Co-Cl-β’** (Figure 2d). A drop in water uptake (of 1 wt %) was observed above 60 % RH. Such negative adsorption beyond a previously equilibrated isotherm point has been previously reported, and is typically a result of guest-induced phase transformation that involves reduction of unit cell volume.[30a,b] Indeed, PXRD after the DVS experiment indicated a different phase, **sql-bib-Co-Cl-γ**, and loss of crystallinity compared to the other phases of **sql-bib-Co-Cl** (Figure S14). The same phase can be obtained when soaking **sql-bib-Co-Cl-α** in water or exposing **sql-bib-Co-Cl-α** to humid air (ca. 60 % RH) for 1 week (Figure S14). The presence of water in **sql-bib-Co-Cl-γ** was also evident from TGA, DSC and FTIR data (Figures S10, S15–S16). Both TGA and DSC data indicate that the water loss is not complete until 400 K, significantly higher than water release from **sql-bib-Co-Cl-β′** (333 K). However, VT PXRD under vacuum showed that, after heating **γ** above 400 K, the initial activated phase **β** could not be obtained (Figure S17). This indicates that the water-induced phase transformation is irreversible under these conditions, as further evidenced by the incomplete water desorption observed during the DVS experiment. FTIR on the **γ** phase indicated the presence of two types of OH stretch vibrations, with overlapping peaks at 3438 and 3394 cm^{-1} (Figure S10). Although attempts to obtain structural information on this phase were unsuccessful, it is plausible that chloro ligands are replaced by aqua ligands above 60 % RH, given that aqua ligands have a higher field strength. The slight change in color from pale purple (**β**) to pink (**γ** and **α**) suggests that the coordination number remained the same (Figure S18). Pawley refinement of a PXRD pattern recorded for **sql-bib-Co-Cl-γ** in air revealed a 9.1 % reduction in unit cell volume compared to **sql-bib-Co-Cl-β** (2292 Å^3 *vs.* 2523 Å^3; Figure S19 and Table S3), which aligns with the experimental observations during water sorption.

Gas Sorption

Activation of **sql-bib-Co-Cl-α** prior to gas sorption was performed under dynamic vacuum at 333 K to afford **sql-bib-Co-Cl-β**. CO_2 sorption at cryogenic conditions (195 K) revealed an S-shaped isotherm (type F-IV) with a gate-opening pressure of 27.7 kPa (Figure 4a). The saturation uptake reached 92.9 $cm^3 g^{-1}$ at 91.4 kPa, corresponding to two CO_2 molecules per Co unit, which matches the MeOH content in as-synthesized **sql-bib-Co-Cl-α** (Table S4). Negli-

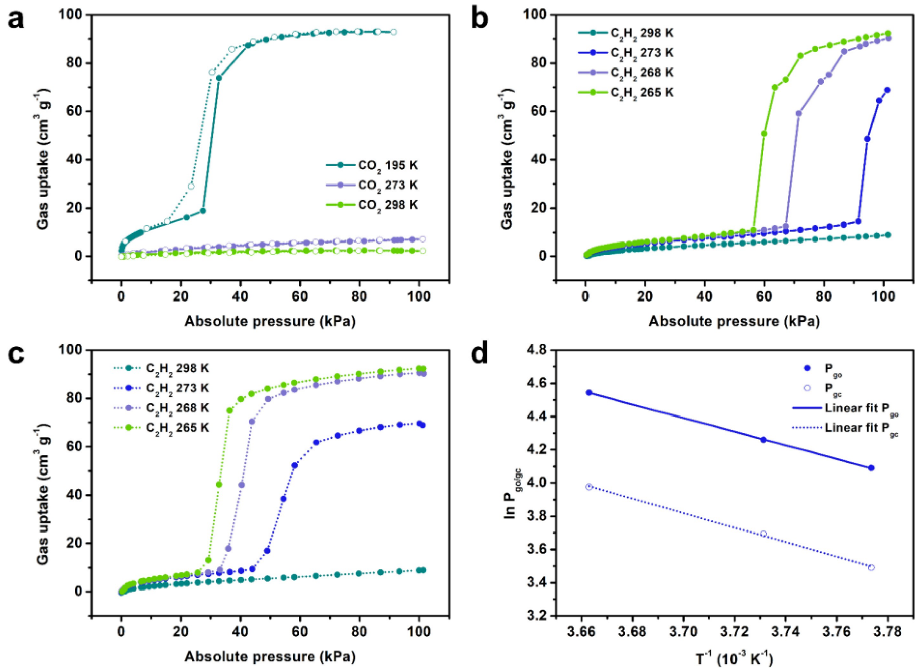

Figure 4. (a) CO_2 sorption isotherms at 195 K (cyan), 273 K (purple) and 298 K (green). C_2H_2 adsorption (b) and desorption (c) isotherms at 298 K (cyan), 273 K (blue), 268 K (purple) and 265 K (green). (d) Van't Hoff plots for gate-opening (full circles) and gate-closing (open circles) pressures for C_2H_2.

gible CO_2 uptake was observed at 273 and 298 K, supporting the absence of open pores in **sql-bib-Co-Cl-β**. S-shaped isotherms were also observed for C_2H_2 at 273, 268 and 265 K with hysteresis ranging from 43 to 45 % (Table S5), while negligible uptake was recorded at 298 K (Figures 4b and 4c). The corresponding gate-opening (and gate-closing) pressures at 273, 268 and 265 K were recorded at 94.0 (53.3), 70.8 (40.2) and 59.8 (32.8) kPa, respectively. The C_2H_2 uptake at 265 K and 101.5 kPa matched that of CO_2, with two molecules of C_2H_2 (or CO_2) per Co unit, consistent with their similar molecular shapes and kinetic diameters (Table S6).[31] The temperature dependence of the gate-opening and gate-closing pressures describing the phase transformation can be determined using the Clausius-Clapeyron equation.[32] Van't Hoff plots (Figure 4d) demonstrate the linear relationship between T^{-1} and lnP for gate-opening or gate-closing (Tables S7–S9). This analysis indicates an enthalpy of adsorption for C_2H_2 of 34.9±0.3 kJ/mol. No gate-opening was observed for N_2 at 77 K or for other gases (CH_4, C_2H_4, C_2H_6, C_3H_4, C_3H_6, C_3H_8) at 273 K (Figures S20–S23). O_2 sorption was also investigated due to its abundance in air and its potential involvement in the phase transformations of **sql-bib-Co-Cl**. O_2 isotherms recorded at 77 K and 298 K reveal negligible uptake at both temperatures (Figure S24), inidcating that O_2 does not induce gate-opening when **sql-bib-Co-Cl** is exposed to air. These results are consistent with the presence of discrete voids in **sql-bib-Co-Cl-β**, which are inaccessible to gases with larger kinetic diameters than CO_2 and C_2H_2 (3.3 Å). PXRD diffractograms recorded after low-pressure sorption confirmed that the sample remained stable as its **sql-bib-Co-Cl-β** or **sql-bib-Co-Cl-β′** forms when exposed to air (Figure S25). These sorption studies collectively demonstrate preferential adsorption of C_2H_2 over CO_2, as evidenced by the gate-opening behavior observed for C_2H_2 at 273 K, which does not occur for CO_2 at the same temperature (Figures 4a and 4b). While **sql-bib-Co-Cl** cannot be explored further for this application due to its irreversible phase transformation under humidity levels exceeding 60 % RH (Figure S12), these findings highlight the potential utility of transiently porous CNs in separation processes. In particular, the confined closed-pore environment within such CNs could enhance host–guest interactions compared to porous or flexible CNs that adsorb gas molecules in open pores (Figure 1). This characteristic may make transient porosity advantageous for gas purification applications.

Motivated by the response of **sql-bib-Co-Cl** to low-pressure CO_2 sorption at cryogenic temperatures, we investigated high-pressure CO_2 sorption at ambient temperature. Surprisingly, no gate-opening was observed for CO_2 at 298 K, even at pressures up to 4490.6 kPa (Figure S26). At 273 K, gate-opening began at 3090.8 kPa (Figure S27), but remained incomplete due to the limiting saturation pressure (P_0) of CO_2 at that temperature (3471.3 kPa). The isotherm recorded at 195 K revealed that gate-opening began at 0.27 P/P_0. This was not the case for the 273 K measurement (0.89 P/P_0), whereas the same sample exposed to CO_2 at 195 K recorded a gate-opening at 0.27 P/P_0 (Figures S28 and S29). Additionally, while the Van't Hoff plot of P_{go} for CO_2 does not align with the slope of the corresponding P_0 plot, a plot of the extrapolated P_{go} from the 195 K measurement (0.27 P/P_0) does match the slope of the P_0 Van't Hoff plot (Figure S30). Typically, flexible CNs exhibit lower capacities, larger hysteresis loops, and higher gate-opening pressures at higher temperatures, for a given gas.[33a,b,c] In the case of **sql-bib-Co-Cl**, the experimental P_{go} shifted by 69 % compared to the extrapolated value, which is among the most pronounced shifts observed in flexible CNs. Other transiently porous CNs have registered even greater shifts at high temperatures (Table S10). This deviance may be attributed to adsorption occurring at an "overpressure" due to the activation barrier for phase transformation, while the desorption curve follows thermodynamic equilibrium.[34a,b,c] The degree of overpressure is related to temperature, as at higher temperatures the difference between the equilibrium temperature for the phase transformation and the actual temperature decreases, causing the Gibbs free energy to become more positive.[34c]

To further investigate the effect of temperature on the CO_2-induced phase transformation in **sql-bib-Co-Cl**, variable-temperature DSC (VT DSC) experiments were conducted under CO_2 at ambient pressure. Three cycles of CO_2 adsorption followed by desorption under N_2 flow were performed at 198 K to avoid any potential CO_2 deposition (Figure 5a). The DSC trace for the first cycle revealed an exothermic peak upon adsorption and an endothermic peak upon desorption. Upon closer examination of the exothermic peak, a shoulder was observed, suggesting two different signals for CO_2 adsorption (Figure 5b). This is consistent with the isotherms collected at 195 K, where the first signal corresponds to the initial diffusion into **β**, followed by gate-opening to a CO_2-loaded phase. The peak profile was maintained over 3 cycles, indicating reversible CO_2 adsorption in **sql-bib-Co-Cl** (Figure S31). Interestingly, upon increasing the temperature to 203 K, the adsorption peak changed from a relatively sharp peak to a smeared peak over 60 minutes of adsorption (Figure 5). Closer inspection revealed that the second signal appeared as a broad peak, indicating a partial structural transformation, while the signal remained reproducible over three cycles (Figure S32). Repeating the experiment at 208 K revealed only the first signal, corresponding to diffusion into **β**, which aligned with a significantly reduced adsorption capacity compared to 198 K (Figures 4 and S33). These differences in adsorption at different temperatures were also apparent in the integrated DSC exotherms (Figure S34), which displayed lower positive slope and lower integrated area with increase in temperature. After desorption, the sample remained in the **sql-bib-Co-Cl-β** phase, as confirmed by PXRD (Figure S35). To rule out any potential temperature dependence of the host phase, SCXRD on **sql-bib-Co-Cl-β** was measured at both high (298 K) and low (198 K) temperatures, revealing isostructural phases at the two temperatures (Figure S36 and Table S11). These findings indicate that the gate-opening phenomenon in **sql-bib-Co-Cl** is temperature-sensitive and does not occur above 208 K up to 1 bar of CO_2 pressure.

In Situ SCXRD

In situ SCXRD under CO_2 pressure was conducted in an environmental cell to gain insight into the structural transformation triggered by CO_2, as described above (see Supporting Information for experimental details). A dataset for the evacuated crystal was collected at 298 K, which matched the previously collected data from a crystal of **sql-bib-Co-Cl-β** at the same temperature (i.e. in the absence of the environment cell, Table S12). Upon CO_2 loading at 40 bar (298 K) and subsequent cooling to 253 K, a phase transformation to a new phase was observed (Figure 6a). The unit cell volume increased from 2540.1(6) Å^3 to 2636.1 (6) Å^3, enlarging the void volume by 27 % (194 to 246 A^3). A comparison of the calculated PXRD patterns for **β** and **β** upon CO_2 loading revealed a shift of the (002) planes (Figure S37), concomitant with a change in the Co–Co distance from 8.660 to 8.707 Å resulting from an elongation of the cavity in the crystallographic *bc* plane (Figures 6b and 6c). Although CO_2 could not be crystallographically refined

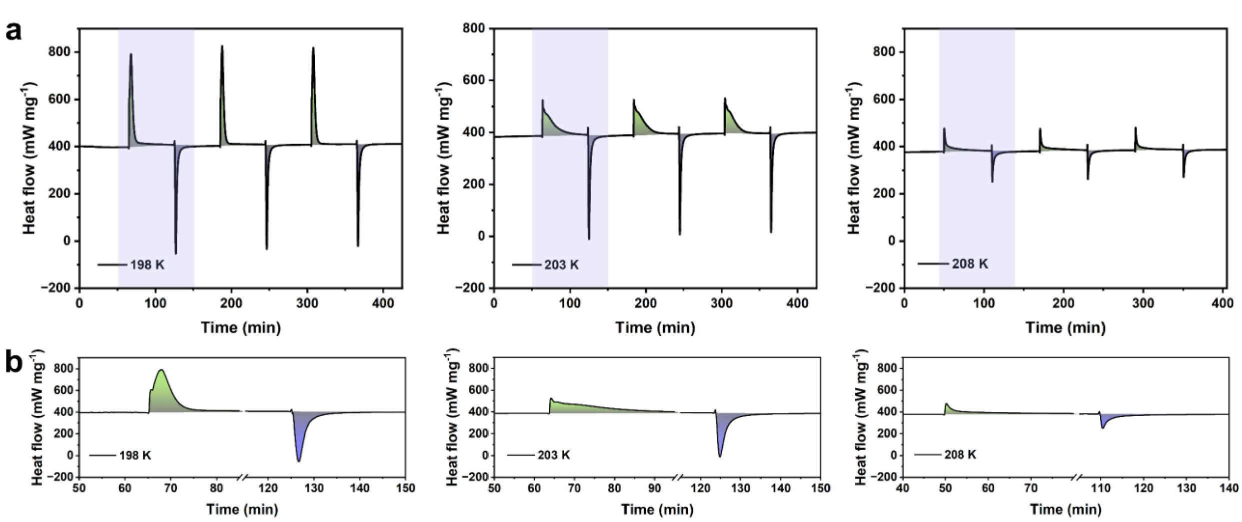

Figure 5. (a) Three differential scanning calorimetry cycles of CO_2 adsorption and desorption (using N_2) recorded at 198, 203 and 208 K. (b) Magnified regions for one cycle corresponding to the shaded areas in (a). Green = adsorption, blue = desorption.

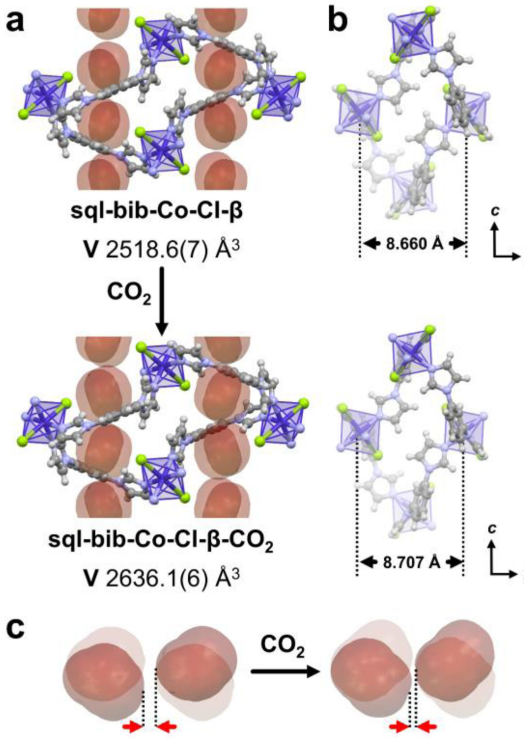

Figure 6. (a) Structural transformation from **sql-bib-Co-Cl-β** to **sql-bib-Co-Cl-CO$_2$**, (b) elongation of Co–Co distances and (c) change in voids in **sql-bib-Co-Cl-β** upon CO$_2$ loading.

due to disorder, an electron density map indicated its presence at the center of the cavities (Figure S38). These positions align with those of MeOH in **sql-bib-Co-Cl-α**, which is unsurprising given the similar molecular volumes of MeOH and CO$_2$ (Figure S13). While this experiment revealed the structure of the host under CO$_2$ at these equilibrated conditions, the mechanism of transient porosity could not be explained from the crystallographic analysis.

Since **sql-bib-Co-Cl-β** adsorbed both CO$_2$ and C$_2$H$_2$, there must be a diffusion mechanism to access the voids. Upon analyzing the voids in both the guest-loaded (**sql-bib-Co-Cl-α**) and guest-free (**sql-bib-Co-Cl-β**) forms, it becomes evident that guest diffusion can be blocked along the crystallographic *ab* plane (Figure 7a). The voids are disconnected by the positioning of the central phenyl ring of the bib linker, with the limiting distance between opposite phenyl rings of 4.188 and 4.059 Å in **sql-bib-Co-Cl-α** and **sql-bib-Co-Cl-β**, respectively (Figure 7b). Therefore, it can be inferred that rotation of this ring could temporarily create a connection between adjacent voids, transiently forming a narrow pore. However, this configuration is sterically hindered due to obstructing hydrogen orientation from the imidazole rings.

To support this possibility, a CSD survey (version 2024.2.0) was conducted on the conformations of the linker bib in CNs. Specifically, the two N–N–C–C torsion angles of the linker were calculated with respect to the distance between the C$_2$ carbons of imidazole rings (Figure 7c). As highlighted in our previous work,[24] the configurations of bib can be summarized into three main categories based on the C–C distance (Figure 7d): (a) *syn*- endo (below ca. 5.75 Å); (b) *anti*- (between ca. 5.75 and 6.75 Å); (c) *syn*- exo (above 6.75 Å). For the *anti*- configuration, as is the case in **sql-bib-Co-Cl**, the torsion angles are divided into two groups, with one imidazole ring at 0–30° relative to the central ring and the other between 90–120° (Figure 7e). For comparison, a C–C distance of 6.084(3) or 6.01(2) Å between the C$_2$ carbons of imidazole rings was measured in **sql-bib-Co-Cl-α** and **sql-bib-Co-Cl-β**, respectively. In both cases, bib adopted an asymmetrical configuration with torsion angles of $-22.8(7)/108.4(5)°$ and $-36(4)/99(3)°$ for **sql-bib-Co-Cl-α** and **sql-bib-Co-Cl-β**, respectively. Therefore, a rotation of the central phenyl ring away from the voids would increase or decrease the respective torsion angles, bringing bib closer to an unfavourable regime of orientations (Figure 7e). Nonetheless, a small rotation is feasible if the energy penalty is compensated by adsorption of gas molecules involving host–guest interactions. Even small linker rotations would be expected to profoundly impact the voids of transiently porous solids, as their % guest-accessible space is 2–3 times lower than that of switching CNs (Figure S39).

Computational Studies

The cavity windows in **sql-bib-Co-Cl** (pore limiting diameter of 2.05 Å) are smaller than the diameter of CO$_2$ (kinetic diameter of 3.30 Å), which should theoretically prevent adsorbate diffusion. However, experimental observations have shown that both adsorption and diffusion occur, prompting us to address the underlying mechanism for CO$_2$ diffusion in **sql-bib-Co-Cl**. To explore this phenomenon at the atomic level, we employed molecular dynamics (MD) simulations. A supercell (3x3x2) of **sql-bib-Co-Cl-α** was loaded with the experimentally observed uptake of 1 CO$_2$ molecule per cavity, or 8 CO$_2$ molecules per unit cell (see Table S4, Figures S40 and S41). MD calculations using 0.1 fs were performed at a constant temperature (195 K) and pressure (101.325 kPa), while the framework was kept flexible, enabling us to monitor internal molecular rearrangements that might facilitate diffusion.

During the simulation, we monitored the internal structure of the framework by calculating free volume and surface area, as well as by analyzing the animation outcomes of the MD simulations (Figure 8). The results revealed internal molecular rearrangements occurred within the first ca. 5 ps of the simulation. To closely monitor the framework behavior during these molecular rearrangements, we conducted an additional short 5 ps MD simulation with a 0.01 fs timestep. As shown in Figure 8a, the free volume initially experienced a significant increase followed by a decrease within the first ca. 5 ps, eventually stabilizing at a nearly constant value that is larger than the initial free volume. Similar changes were observed for the surface area, with a steep increase during the first 5 ps (Figure S42). MD simulations suggest an internal molecular rearrangement

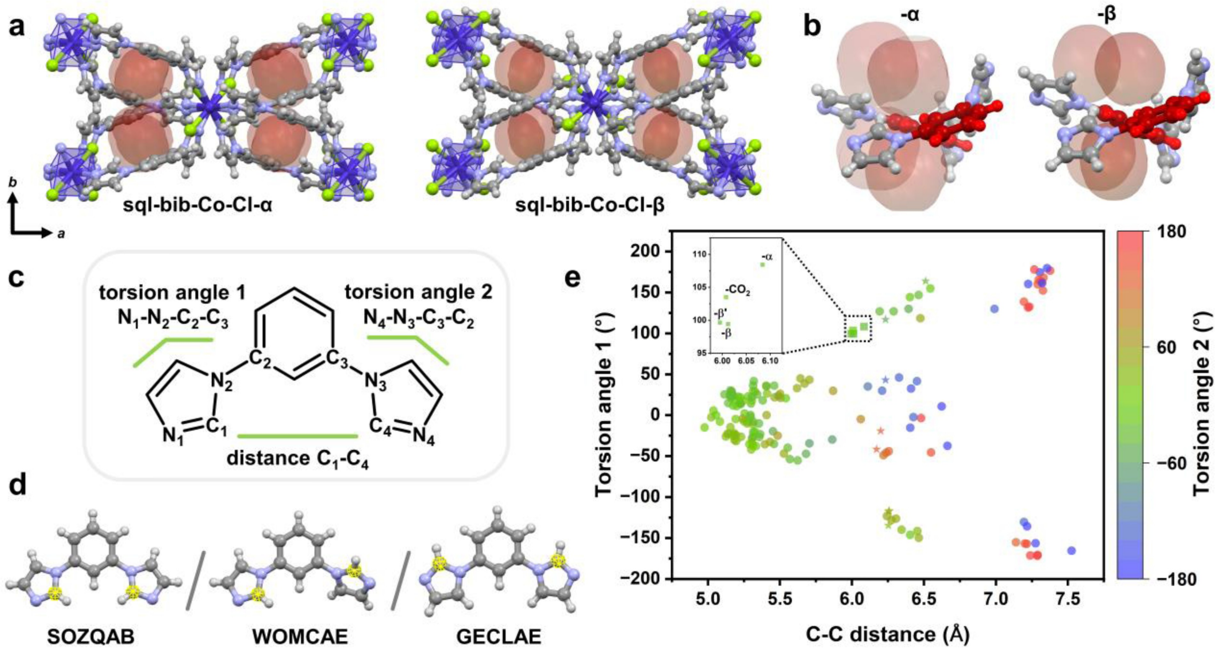

Figure 7. (a) Voids in **sql-bib-Co-Cl-α** and **sql-bib-Co-Cl-β** and (b) orientation of phenyl rings of the linker relative to the voids. (c) Schematic representation of torsion angles 1 and 2 and C–C distance used as an input for the database mining of bib linker configurations. (d) Possible configurations of the linker as exemplified by CSD Refcodes SOZQAB, WOMCAE, GECLAE (highlighted atoms in yellow indicate C–C distances for different configurations). (e) Scatter plot of N–N–C–C torsion angle 1 plotted against C–C (C_1-C_4) distance of bib linker in CNs deposited in the CSD database (version 2024.2.0). Color map represents torsion angle 2 for the same linker. Stars: **X-dmp-1-M** family (refs [10b and c]); circles: rest of CSD; rectangles: **sql-bib-Co-Cl**. Inlet shows magnified area of the black rectangle in the full plot; **α**, **β**, **β'** and CO_2 phases of **sql-bib-Co-Cl** are labelled in the inlet.

process from the XRD-refined and DFT-optimized atomic positions resulting in a structure with a larger free volume, thereby facilitating the diffusion of adsorbates (see Supplementary file, **sql-bib-Co-Cl_CO2.avi**). To examine the internal structural changes during the rearrangement, we calculated the average angle variations $\theta(t)$ between the normal vectors of phenyl rings in the linkers over time (Figures 8b and 8c). As shown in Figure 8b, $\theta(t)$ underwent significant changes during the rearrangement phase before stabilizing at a value greater than zero, and remained stable for simulation times up to 100 ps (Figure S43). This stabilization suggests an internal bib linker rotation that transiently creates open channels/gates, facilitating the diffusion of CO_2. To gain further insight into the internal rearrangement mechanism of the framework, we explored the possibility of linker torsional motion. The angle between the imidazole and phenyl ring with respect to time ($\Phi_1(t)$) revealed a peak within ca. 5 ps, corresponding to the internal rearrangement observed in (Figure S44). This suggests that a significant rotation occurred during this rearrangement process, followed by stabilization at a $\Phi_1(t)$ value larger than its initial state. In contrast, the $\Phi_2(t)$ plot shows no significant change, which could be attributed to the averaging of motions between different linkers. Indeed, the crystal packing of the supercell changed during simulation, with areas exhibiting phenyl ring rotation, as speculated above (Figure S45). To investigate this with respect to torsion angle, individual nets can be examined at different simulation times (t_s): 0.25, 1.6 and 35 ps, respectively (Figures S46 and S47). Each **sql** net underwent torsion angle changes to different extents in each square grid. The torsion angle in the same region of the supercell can be quantified with respect to simulation time (Figure 8d). For the same linker on the same net, we found changes of N–N–C–C torsion angles as follows: 109.34° and −15.57° at 0.25 ps, 82.47° and 23.55° at 1.6 ps, and 133.48° and −26.73° at 35 ps. These torsion angles indicate that linker orientation is similar at $t_s = 0.25$ and 35 ps, but different at 1.6 ps where the framework undergoes significant rearrangement due to symmetry breaking and guest diffusion. These torsion angles along with respective M–M distances were quantified for the same simulation times for four consecutive square grids in each net (Figures S48–S51). Both torsion angles and M–M distances for each net were found to typically differ for $t_s = 1.6$ ps, while they were similar at $t_s = 0.25$ and 35 ps, being consistent with previous observations of the isolated investigated linker. Further, to better illustrate the transient porosity mechanism, we inspected three consecutive ligands around a CO_2 molecule that travels from one cavity to another, at relevant simulation times: 0.25, 1.6, 1.85, 2.25, 15, 35 ps (Figure 8e). We observed that the process is facilitated by continuous torsion angle change of the nearby ligands. During the first 1.85 ps, the CO_2 molecule is closest to the chloro ligand pointing towards the top cavity (Figure 8e), with C_{CO2}–Cl_1 distances of 3.74, 3.25, and 3.44 Å at times $t_s = 0.25$, 1.6, and 1.85 ps, respectively. Starting from 2.25 ps, the CO_2 molecule moves further away from this chloro ligand (C_{CO2}–Cl_1 distances of 3.78, 4.94, and 4.74 Å at times $t_s = 2.25$, 15, and

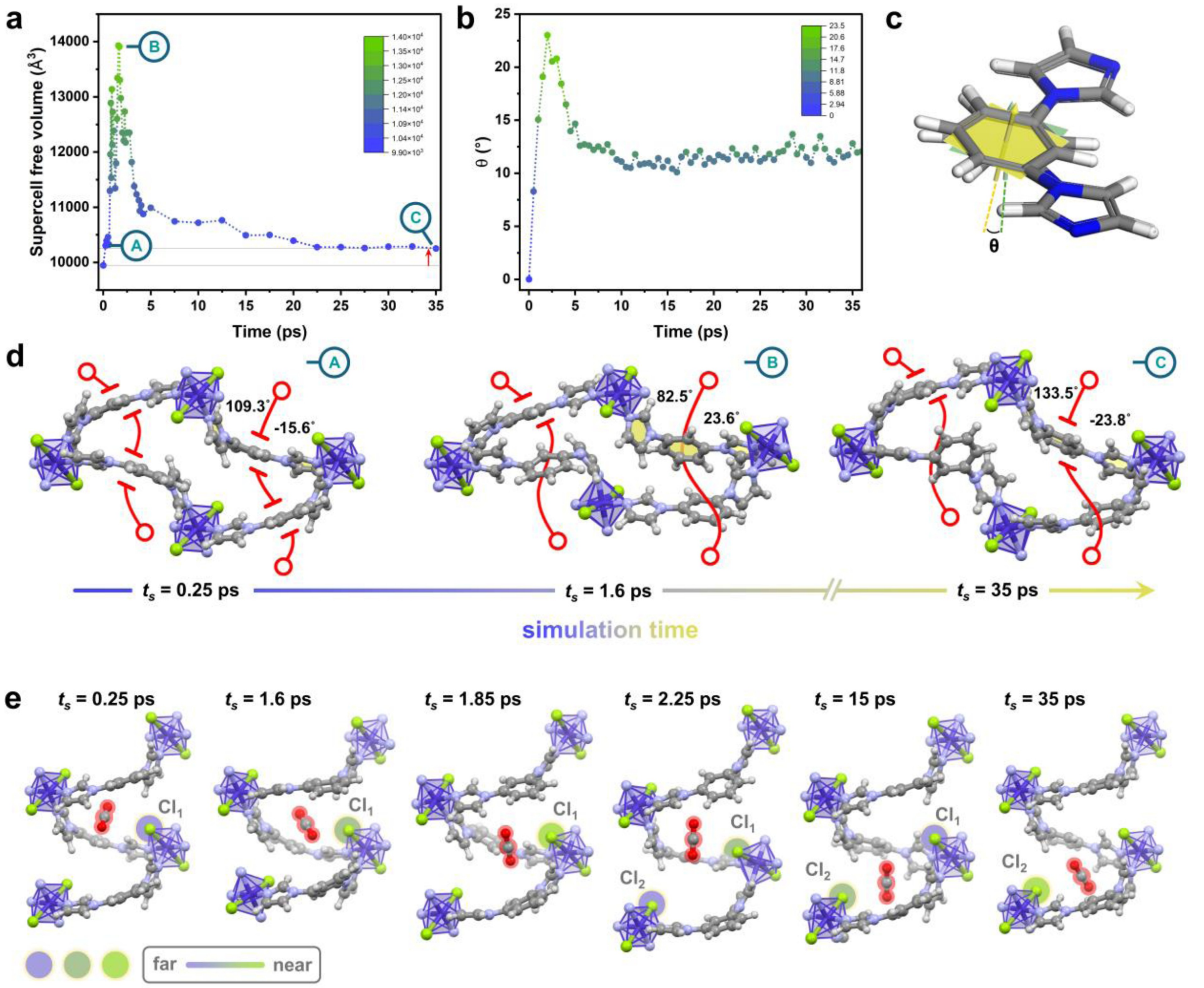

Figure 8. Change in free volume of **sql-bib-Co-Cl** (results are shown for simulations using timesteps of 0.1 fs (spanning 0 to 35 ps) and 0.01 fs (spanning 0 to 5 ps)) (a) and angle θ (b) during molecular dynamic (MD) simulations upon CO_2 diffusion, plotted against simulation time. Red arrow in (a) indicates increase in supercell free volume upon CO_2 loading. (c) The angle θ between the normal vector of the phenyl ring plates at time t and the normal vector of the ring plates at the initial time (time 0). (d) Crystal packing along crystallographic *c* axis of the same region at simulation times of 0.25 ps (A), 1.6 ps (B) and 35 ps (C). Connecting of cavities is shown with red lines and torsion angles around one linker are noted. (e) Illustration of the transient porosity process for one CO_2 molecule highlighted in red. Colored circles indicate the distance between the C atom of the CO_2 molecule and nearby chloro ligands (far = purple; near = green).

35 ps, respectively) and closer to the opposite chloro ligand that points towards the bottom cavity (Figure 8e). The CO_2 molecule progressively moves closer into the cavity, until reaching its final position at 35 ps (C_{CO2}–Cl_2 distances of 5.64, 3.62, and 3.79 Å at times t_s = 2.25, 15, and 35 ps, respectively). The torsion angles of all three nearby ligands experience changes, indicating that the transient porosity process is collective for adjacent cavities (Figures S52–S54). However, the ligand in between the two cavities undergoes the most extreme transformations, with torsion angles ranging from 150.36°/-31.58° at 1.6 ps and 109.43°/-14.99° at 35 ps. Overall, this analysis suggests that, when comparing the framework of **sql-bib-Co-Cl** before and after gas diffusion, a pathway for guest diffusion can be realized, transiently connecting the spaces between adjacent cavities through linker rotation.

In comparison to other transiently porous CNs, the arrangement of voids and mechanism of guest transport are similar. For instance, cavities are sectioned by benzene pendant rings on the carboxylate linker in the **X-dmp-1-M** family[10b,c] or by a naphthalene moiety in **[$Co_2(ndc)_2(bpy)]_n$**.[10a] In both cases, guest transport is enabled via the rotation of the aromatic moieties on the linkers, functioning as a type of turnstile. Notably, although the primary transport mechanism in **X-dmp-1-Co** involves the carboxylate linker,[10b] we hypothesized that the secondary ligand bib may also undergo some conformational changes. Indeed, the N–N–C–C torsion angles of bib change from −45(1)/117.6(7)° in the as-synthesized phase to −31(1)/127.0(6)° in the activated phase. This results in a 14±2° and 9.4±1.3° rotation for each imidazole ring, almost the same as the rotation occurring for **sql-bib-Co-Cl** (13.2±4.7° and 9.4 ±3.5°). While **sql-bib-Co-Cl** is a 2D CN with π–π stacking of bib linkers between adjacent layers, **X-dmp-1-Co** is a 3D CN where the bib linkers are spatially separated. Instead, π–π stacking in **X-dmp-1-Co** occurs between bib and carboxylate ligands, with the centroid-centroid distance reducing from 4.026 Å to 3.775 Å after activation. In comparison, π–π interactions decrease from 4.105 Å in **sql-bib-Co-Cl-α** to 3.851 Å in **sql-bib-Co-Cl-β**. Both materials show a 0.25 Å decrease in π–π distances. These similarities suggest that transient porosity could be a designable feature in CNs based on bib. To explore this further, we revisited our CSD survey on CNs sustained by bib, revealing that 30 hits contain clathrated solvent (Table S13). Besides the **X-dmp-1-M** family, none of these have been studied for gas sorption, despite several having relatively high void space and low pore limiting diameters. This analysis highlights how bib and linkers with similar features might offer an opportunity for transient porosity by design.

Conclusion

In conclusion, we report a transiently porous CN, **sql-bib-Co-Cl**, that exhibits gas- and vapor-induced phase transformations between closed pore phases and preferential sorption of C_2H_2 over CO_2 and other C2 gases. Gas sorption experiments showed stepped isotherms for CO_2 and C_2H_2, while in situ SCXRD revealed that guest molecules occupy cavities within the structure. MD simulations provide insight into the mechanism of guest diffusion, and indicate that the nature of the linker is key to enabling transient porosity by temporarily creating connections between adjacent cavities through phenyl ring rotation. This study serves as a proof of concept for the development of other closed pore CNs that exhibit transient porosity and suggests utility in separations. With respect to the latter, the humidity-induced irreversible phase transformation of **sql-bib-Co-Cl** renders it unsuitable for separation studies. With respect to the former, the use of bent linkers similar to bib in **sql-bib-Co-Cl** may promote this behavior through rotational flexibility, particularly when the linkers are aligned in an inverse fashion. The deliberate design of transiently porous CNs remains a challenge, but may begin with a search for existing CNs exhibiting similar torsion angles to those observed in **sql-bib-Co-Cl**. Such investigations are currently underway, with the aim of enabling crystal engineers and materials chemists to find more "*needles in a haystack*".

Supporting Information

CCDC 2394385–2394391 contain the supplementary crystallographic data for this paper. These data can be obtained free of charge via www.ccdc.cam.ac.uk/data_request/cif, or by emailing data_request@ccdc.cam.ac.uk, or by contacting The Cambridge Crystallographic Data Centre, 12 Union Road, Cambridge CB2 1EZ, UK; fax: +44 1223 336 033.

The following files are available free of charge.

Materials and Methods, Supporting Tables and Figures (PDF)

DFT-optimized structure of sql-bib-Co-Cl-α (CIF)

DFT-optimized structure of sql-bib-Co-Cl-β' (CIF)

Movie of MD Simulations sql-bib-Co-Cl_CO2 (AVI)

Author Contributions

The manuscript was written through contributions of all authors. All authors have given approval to the final version of the manuscript.

CRediT: K.K.: conceptualization, investigation, visualization, writing – original draft; A.C.E, D.S., S. M.: investigation, writing – review & editing; M. L., T. H.: resources, writing – review & editing; S. J.-N. and M. V.: formal analysis, writing – review & editing; L. J. B.: methodology, resources, writing – review & editing; M. J. Z.: supervision, writing – review & editing.

Acknowledgements

M.J.Z. acknowledges the financial support from the Science Foundation Ireland (16/IA/4624) and the European Research Council (ADG 885695). S.M. acknowledges an SFI-IRC Pathway award (21/PATH-S/9454). S.J.N. and M.V. acknowledge the Irish Center for High-End Computing (ICHEC). S.J.N. thanks Enterprise Ireland and the European Union's Horizon 2020 research and innovation programme under the Marie Skłodowska-Curie grant agreement 847402 (ID: MF20210297).

Conflict of Interest

The authors declare no conflict of interest.

Data Availability Statement

The data that support the findings of this study are available from the corresponding author upon reasonable request.

Keywords: transient porosity · phase transformation · coordination network · crystal engineering

---

[1] a) S. Kitagawa, R. Kitaura, S.-i. Noro, *Angew. Chem. Int. Ed.* **2004**, *43*, 2334–2375; b) W. Fan, X. Zhang, Z. Kang, X. Liu, D. Sun, *Coord. Chem. Rev.* **2021**, *443*, 213968; c) Z. Chen, K. O. Kirlikovali, K. B. Idrees, M. C. Wasson, O. K. Farha, *Chem* **2022**, *8*, 693–716; d) X. Zhang, J. Maddock, T. M. Nenoff, M. A. Denecke, S. Yang, M. Schröder, *Chem. Soc. Rev.* **2022**, *51*, 3243–3262.

[2] a) R. L. Siegelman, E. J. Kim, J. R. Long, *Nature Materials* **2021**, *20*, 1060–1072; b) J.-H. Li, Y.-W. Gan, J.-X. Chen, R.-B. Lin, Y. Yang, H. Wu, W. Zhou, B. Chen, X.-M. Chen, *Angew. Chem. Int. Ed.* **2024**, *63*, e202400823; c) A. Cadiau, K. Adil, P. M. Bhatt, Y. Belmabkhout, M. Eddaoudi, *Science* **2016**, *353*, 137–140.

[3] a) L. J. Barbour, *Chem. Commun.* **2006**, 1163–1168; b) D. Holden, S. Y. Chong, L. Chen, K. E. Jelfs, T. Hasell, A. I. Cooper, *Chem. Sci.* **2016**, *7*, 4875–4879.

[4] a) S. Zhou, O. Shekhah, A. Ramírez, P. Lyu, E. Abou-Hamad, J. Jia, J. Li, P. M. Bhatt, Z. Huang, H. Jiang, T. Jin, G. Maurin, J. Gascon, M. Eddaoudi, *Nature* **2022**, *606*, 706–712; b) K.-J. Chen, D. G. Madden, S. Mukherjee, T. Pham, K. A. Forrest, A. Kumar, B. Space, J. Kong, Q.-Y. Zhang, M. J. Zaworotko, *Science* **2019**, *366*, 241–246.

[5] J. Rouquerol, D. Avnir, C. W. Fairbridge, D. H. Everett, J. M. Haynes, N. Pernicone, J. D. F. Ramsay, K. S. W. Sing, K. K. Unger, *Pure Appl. Chem.* **1994**, *66*, 1739–1758.

[6] J. Tian, P. K. Thallapally, B. P. McGrail, *CrystEngComm* **2012**, *14*, 1909–1919.

[7] S. Allison, R. Barrer, *J. Chem. Soc. A* **1969**, 1717–1723.

[8] a) J. L. Atwood, L. J. Barbour, A. Jerga, B. L. Schottel, *Science* **2002**, *298*, 1000–1002; b) J. L. Atwood, L. J. Barbour, A. Jerga, *Angew. Chem. Int. Ed.* **2004**, *43*, 2948–2950; c) P. K. Thallapally, T. B. Wirsig, L. J. Barbour, J. L. Atwood, *Chem. Commun.* **2005**, 4420–4422.

[9] a) P. K. Thallapally, B. Peter McGrail, S. J. Dalgarno, H. T. Schaef, J. Tian, J. L. Atwood, *Nature Materials* **2008**, *7*, 146–150; b) J. A. Riddle, J. C. Bollinger, D. Lee, *Angew. Chem. Int. Ed.* **2005**, *44*, 6689–6693.

[10] a) D. P. van Heerden, V. J. Smith, H. Aggarwal, L. J. Barbour, *Angew. Chem. Int. Ed.* **2021**, *60*, 13430–13435; b) V. I. Nikolayenko, D. C. Castell, D. Sensharma, M. Shivanna, L. Loots, K. A. Forrest, C. J. Solanilla-Salinas, K.-i. Otake, S. Kitagawa, L. J. Barbour, B. Space, M. J. Zaworotko, *Nat. Chem.* **2023**, *15*, 542–549; c) V. I. Nikolayenko, D. C. Castell, D. Sensharma, M. Shivanna, L. Loots, K.-i. Otake, S. Kitagawa, L. J. Barbour, M. J. Zaworotko, *J. Mater. Chem. A* **2023**, *11*, 16019–16026.

[11] a) Q.-Y. Yang, P. Lama, S. Sen, M. Lusi, K.-J. Chen, W.-Y. Gao, M. Shivanna, T. Pham, N. Hosono, S. Kusaka, J. J. Perry IV, S. Ma, B. Space, L. J. Barbour, S. Kitagawa, M. J. Zaworotko, *Angew. Chem. Int. Ed.* **2018**, *57*, 5684–5689; b) L. Abylgazina, I. Senkovska, S. Kaskel, *Commun. Mater.* **2024**, *5*, 132; c) S. Horike, S. Shimomura, S. Kitagawa, *Nat. Chem.* **2009**, *1*, 695–704.

[12] J. A. Mason, J. Oktawiec, M. K. Taylor, M. R. Hudson, J. Rodriguez, J. E. Bachman, M. I. Gonzalez, A. Cervellino, A. Guagliardi, C. M. Brown, P. L. Llewellyn, N. Masciocchi, J. R. Long, *Nature* **2015**, *527*, 357–361.

[13] S. Subramanian, M. J. Zaworotko, *Angew. Chem. Int. Ed.* **1995**, *34*, 2127–2129.

[14] a) B. Moulton, M. J. Zaworotko, *Chem. Rev.* **2001**, *101*, 1629–1658; b) G. R. Desiraju, *Angew. Chem. Int. Ed.* **2007**, *46*, 8342–8356; c) S. Mukherjee, M. J. Zaworotko, *Trends Chem.* **2020**, *2*, 506–518.

[15] a) C. B. Aakeröy, N. R. Champness, C. Janiak, *CrystEngComm* **2010**, *12*, 22–43; b) A. Schoedel, L. Wojtas, S. P. Kelley, R. D. Rogers, M. Eddaoudi, M. J. Zaworotko, *Angew. Chem. Int. Ed.* **2011**, *50*, 11421–11424.

[16] S.-Q. Wang, S. Mukherjee, M. J. Zaworotko, *Faraday Discuss.* **2021**, *231*, 9–50.

[17] a) K. Koupepidou, V. I. Nikolayenko, D. Sensharma, A. A. Bezrukov, M. Vandichel, S. J. Nikkhah, D. C. Castell, K. A. Oyekan, N. Kumar, A. Subanbekova, W. G. Vandenberghe, K. Tan, L. J. Barbour, M. J. Zaworotko, *J. Am. Chem. Soc.* **2023**, *145*, 10197–10207; b) K. Koupepidou, V. I. Nikolayenko, D. Sensharma, A. A. Bezrukov, M. Shivanna, D. C. Castell, S.-Q. Wang, N. Kumar, K.-i. Otake, S. Kitagawa, M. J. Zaworotko, *Chem. Mater.* **2023**, *35*, 3660–3670.

[18] a) A. Schneemann, P. Vervoorts, I. Hante, M. Tu, S. Wannapaiboon, C. Sternemann, M. Paulus, D. C. F. Wieland, S. Henke, R. A. Fischer, *Chem. Mater.* **2018**, *30*, 1667–1676; b) S. Ehrling, M. Mendt, I. Senkovska, J. D. Evans, V. Bon, P. Petkov, C. Ehrling, F. Walenszus, A. Pöppl, S. Kaskel, *Chem. Mater.* **2020**, *32*, 5670–5681.

[19] M. Maliuta, I. Senkovska, V. Romaka, M. Roslova, Z. Huang, P. Petkov, V. Bon, S. Kaskel, *CCS Chemistry* **2023**, *5*, 2225–2236.

[20] a) X.-J. Yang, Q.-L. Zhang, *Z. Anorg. Allg. Chem.* **2016**, *642*, 1158–1165; b) D. Wu, K. Wang, H. Ma, H. Pang, T. Yu, Z. Zhang, S. Li, H. Liu, *Solid State Sci.* **2014**, *35*, 39–44.

[21] L. Schlechte, V. Bon, R. Grünker, N. Klein, I. Senkovska, S. Kaskel, *Polyhedron* **2012**, *44*, 179–186.

[22] J. Pang, F. Jiang, D. Yuan, J. Zheng, M. Wu, G. Liu, K. Su, M. Hong, *Chem. Sci.* **2014**, *5*, 4163–4166.

[23] L. Zhu, H.-R. Li, Y.-N. Mao, R. Liu, B. Zhang, J. Chen, W. Xu, L. Zhang, C.-P. Li, *Chin. Chem. Lett.* **2024**, *35*, 109921.

[24] K. Koupepidou, A. A. Bezrukov, D. C. Castell, D. Sensharma, S. Mukherjee, M. J. Zaworotko, *Chem. Commun.* **2023**, *59*, 13867–13870.

[25] a) C. Shen, T. Sheng, Q. Zhu, S. Hu, X. Wu, *CrystEngComm* **2012**, *14*, 3189–3198; b) S.-J. Fu, C.-Y. Cheng, K.-J. Lin, *Crystal Growth and Design* **2007**, *7*, 1381–1384.

[26] a) H. Grime, J. A. Santos, *Z. Kristallogr. Cryst. Mater* **1934**, *88*, 136–141; b) A. Wojakowska, E. Krzyżak, S. Plińska, *J. Therm. Anal. Calorim.* **2007**, *88*, 525–530.

[27] V. Bon, N. Kavoosi, I. Senkovska, S. Kaskel, *ACS Applied Materials and Interfaces* **2015**, *7*, 22292–22300.

[28] K. S. Sing, *Pure Appl. Chem.* **1985**, *57*, 603–619.

[29] D. P. van Heerden, L. J. Barbour, *Chem. Soc. Rev.* **2021**, *50*, 735–749.

[30] a) S. Krause, V. Bon, I. Senkovska, U. Stoeck, D. Wallacher, D. M. Többens, S. Zander, R. S. Pillai, G. Maurin, F.-X. Coudert, S. Kaskel, *Nature* **2016**, *532*, 348–352; b) D. O'Nolan, A. Kumar, M. J. Zaworotko, *J. Am. Chem. Soc.* **2017**, *139*, 8508–8513.

[31] J. Wang, Y. Zhang, Y. Su, X. Liu, P. Zhang, R.-B. Lin, S. Chen, Q. Deng, Z. Zeng, S. Deng, B. Chen, *Nat. Commun.* **2022**, *13*, 200.

[32] M. Ichikawa, A. Kondo, H. Noguchi, N. Kojima, T. Ohba, H. Kajiro, Y. Hattori, H. Kanoh, *Langmuir* **2016**, *32*, 9722–9726.

[33] a) A. Boutin, F.-X. Coudert, M.-A. Springuel-Huet, A. V. Neimark, G. Férey, A. H. Fuchs, *J. Phys. Chem. C* **2010**, *114*, 22237–22244; b) S. Rahman, A. Arami-Niya, X. Yang, G. Xiao, G. Li, E. F. May, *Commun. Chem.* **2020**, *3*, 186; c) B. Russell, J. Villaroel, K. Sapag, A. D. Migone, *J. Phys. Chem. C* **2014**, *118*, 28603–28608.

[34] a) S. Watanabe, H. Sugiyama, H. Adachi, H. Tanaka, M. T. Miyahara, *J. Chem. Phys.* **2009**, *130*; b) F.-X. Coudert, M. Jeffroy, A. H. Fuchs, A. Boutin, C. Mellot-Draznieks, *J. Am. Chem. Soc.* **2008**, *130*, 14294–14302; c) J. D. Evans, V. Bon, I. Senkovska, H.-C. Lee, S. Kaskel, *Nat. Commun.* **2020**, *11*, 2690.

Manuscript received: December 2, 2024
Accepted manuscript online: January 21, 2025
Version of record online: February 14, 2025